

Ion and impurity transport in turbulent, anisotropic magnetic fields

This article has been downloaded from IOPscience. Please scroll down to see the full text article.

2011 Plasma Phys. Control. Fusion 53 085022

(<http://iopscience.iop.org/0741-3335/53/8/085022>)

View [the table of contents for this issue](#), or go to the [journal homepage](#) for more

Download details:

IP Address: 94.68.151.2

The article was downloaded on 24/06/2011 at 12:13

Please note that [terms and conditions apply](#).

Ion and impurity transport in turbulent, anisotropic magnetic fields

M Negrea¹, I Petrisor¹, H Isliker², A Vogianou², L Vlahos² and B Weysow^{3,4}

¹ Department of Physics, Association Euratom-MEdC, Romania, University of Craiova, A.I. Cuza str. 13, Craiova, Romania

² Section of Astrophysics, Astronomy and Mechanics, Department of Physics, University of Thessaloniki, Association Euratom-Hellenic Republic, 541 24 Thessaloniki, Greece

³ Physique Statistique-Plasmas, Association Euratom-Etat Belge, Université Libre de Bruxelles, Campus Plaine, Bd. du Triomphe, 1050 Bruxelles, Belgium

⁴ EFDA-CSU, D-85748 Garching, München, Germany

Received 4 December 2010, in final form 20 May 2011

Published 23 June 2011

Online at stacks.iop.org/PPCF/53/085022

Abstract

We investigate ion and impurity transport in turbulent, possibly anisotropic, magnetic fields. The turbulent magnetic field is modeled as a correlated stochastic field, with Gaussian distribution function and prescribed spatial auto-correlation function, superimposed onto a strong background field. The (running) diffusion coefficients of ions are determined in the three-dimensional environment, using two alternative methods, the semi-analytical decorrelation trajectory (DCT) method, and test-particle simulations. In a first step, the results of the test-particle simulations are compared with and used to validate the results obtained from the DCT method. For this purpose, a drift approximation was made in slab geometry, and relatively good qualitative agreement between the DCT method and the test-particle simulations was found. In a second step, the ion species He, Be, Ne and W, all assumed to be fully ionized, are considered under ITER-like conditions, and the scaling of their diffusivities is determined with respect to varying levels of turbulence (varying Kubo number), varying degrees of anisotropy of the turbulent structures and atomic number. In a third step, the test-particle simulations are repeated without drift approximation, directly using the Lorentz force, first in slab geometry, in order to assess the finite Larmor radius effects, and second in toroidal geometry, to account for the geometric effects. It is found that both effects are important, most prominently the effects due to toroidal geometry and the diffusivities are overestimated in slab geometry by an order of magnitude.

(Some figures in this article are in colour only in the electronic version)

1. Introduction

One of the central issues for the successful operation of fusion devices is to understand and ultimately control the behavior of ions in the driven, high-temperature, turbulent plasma. Turbulence-induced stochastic magnetic fluctuations, even when small, can destroy the regularly nested magnetic field structures in toroidal confinement devices, such as in tokamaks, which can cause the particles to undergo larger radial displacements. New channels are then opened through which particles can potentially be transported, and transport may become enhanced or even anomalous (see, e.g., [1–3]).

Ions present inside fusion devices include, among others, He-ash (atomic number $Z = 2$) as the fusion product that needs to be prevented from accumulating at the center and should be removed from the device, noble gases such as Ne ($Z = 10$) that help improve confinement through reducing the heat load on the walls by radiating off heat, and undesired impurities such as W ($Z = 74$) that flow in from the wall, and which can degrade confinement substantially when accumulated in the plasma core (see, e.g., [4]).

A number of experimental studies of impurity transport exists, addressing the parameter dependence of ion transport, including the dependence on the atomic number Z and on the logarithmic density and temperature scale lengths, which depend on the device, the plasma mode and the radial location inside the device. For example, [5] investigates the Z -dependence of impurity transport at JET, [6] the anomalous transport of light and heavy impurities in Tore Supra ohmic, weakly saw-toothed plasmas, and [7] compares the parametric dependences of impurity transport in the neoclassical theory with those in turbulence models, also presenting a summary of experimental results and a discussion of the underlying physical mechanisms.

In theoretical studies of impurity transport, several approaches have been used. Test-particle simulations were done in [8,9] for impurities, in [10] for alpha particles in burning plasmas and in [11] for fast particles in a magnetic topology with rotating islands. Gyro-kinetic simulations of impurity transport were performed in [12], as well as in [13] together with fluid simulations, considering electromagnetic effects, and in [14] together with a Fokker–Planck transport model, with transport coefficients taken from the gyro-kinetic simulations. Fülöp and Nordman [15] performed fluid simulations of impurity transport, addressing the Z -scaling, the scaling with normalized logarithmic temperature and density gradients, and applying an ITER scenario. Sánchez Burillo *et al* [16] studied impurity transport with tracers in a two-fluid model, and Reiser *et al* [17] used a Vlasov Fokker–Planck description of impurity transport.

From the mentioned theoretical and experimental studies, it can be concluded that impurity transport is mostly anomalous, the convective velocity and the diffusion coefficients are more than one order of magnitude higher than the neoclassical values (with a few exceptions though where transport is neoclassical, i.e. collisional in toroidal geometry). The parameter dependence of impurity transport coefficients is reported to be rather complex, e.g. whether there is a Z -dependence depends on the concrete device, the plasma mode and the radial location (through the dependence on the logarithmic density and temperature gradient), high- and low- Z impurities scale differently with the logarithmic density gradient, and the diffusion and convection coefficients can become constant at high Z . Also, electron and ion cyclotron heating can affect impurity peaking, e.g. electron heating can reverse the sign of the convective velocity. The anomalous impurity transport is considered to be caused by turbulence and driven by micro-instabilities, most prominently the ion temperature gradient (ITG) and trapped electron mode (TEM) micro-instabilities (see, e.g., [7, 18]).

In this paper, we consider ion and impurity transport in a turbulent magnetic field, with the aim to determine the (running) diffusion coefficients [19] of different ion species. The

turbulent magnetic field is modeled as a correlated stochastic field, with prescribed distribution and spatial auto-correlation function, superimposed onto a strong background magnetic field. To study particle transport, we use two alternative methods. (1) We formulate the problem in terms of the Langevin equations for the guiding centre and apply the semi-analytical method of decorrelation trajectories (DCT), which is a generalization of the Corrsin approximation and does not ignore trapping effects (which necessarily exist in relatively strong turbulent plasmas) [20, 21]. (2) We perform test-particle simulations in numerically generated stochastic magnetic fields. The stochastic fields are generated on a grid such that they have the same statistical properties (distribution and auto-correlation function) as those used in the DCT method.

The particle transport is expected to depend on the level of turbulence and on the spatial, possibly anisotropic, correlations of the stochastic fluctuations, i.e. the appearance of spatially coherent structures in the radial or poloidal direction, such as zonal flows or streamers (see, e.g., [3]). We thus determine the diffusion coefficients for different levels of magnetic turbulence, whose intensity can be measured by the dimensionless magnetic Kubo number K_m (see, e.g., [19, 20, 22–24]), different plasma temperatures (expressed in terms of the dimensionless drift Kubo number K_{dr}) and different degrees of anisotropy in the magnetic fluctuations (described by the stochastic anisotropy parameter Λ). The impurities considered here are He, Be, Ne and W, all assumed to be fully ionized.

The aim of this work is threefold: (i) In the first step, the results of the test-particle simulations are compared with and used to validate the results obtained from the DCT method for the same physical system. For this purpose, we consider a simplifying slab approximation [25], and we use arbitrary values of K_{dr} , for the sake of a more extended parametric study. (ii) In the second step, we determine the running diffusion coefficients of the impurities mentioned above under ITER-like conditions, with realistic values also for K_{dr} , and we perform a parametric study to determine the scaling of the diffusivities with Z , K_m and Λ . (iii) In the third step, we first assess the appropriateness of the guiding center approximation, by comparing with test-particle simulations that directly use the Lorentz force. Second, we explore the importance of geometric effects by comparing with results of test-particle simulations performed in toroidal geometry, with turbulent fluctuations on top of a realistic (vacuum) magnetic background field.

The paper is organized as follows. The Langevin equations for the guiding center of ion drift motion in a stochastic, stationary magnetic field are established in section 2. The results of the DCT method, decorrelation trajectories and running diffusion coefficients, are presented in section 3 (details of the DCT method are given in the appendix). Section 4 contains the test-particle simulations, including the description of how the stochastic fields are constructed, the comparison with the DCT method (section 4.3.1), the parametric study of the diffusivities under ITER-like conditions (section 4.3.2), and the comparison with the case of directly using the Lorentz force, first in slab geometry, and then in toroidal geometry (section 4.3.3). The summary and conclusions are presented in section 5.

2. Equations of motion for the ions in the slab geometry

We consider a shear-less slab geometry for the stationary confining magnetic field with a strong component B_0 along the Z -axis and fluctuating perpendicular components in the (X, Y) -plane,

$$B(\mathbf{X}; Z) = B_0\{e_Z + \beta b_X(\mathbf{X}; Z)e_X + \beta b_Y(\mathbf{X}; Z)e_Y\}, \quad (1)$$

where $\mathbf{X} = (X, Y)$ and β is the dimensionless amplitude of the magnetic field fluctuations relative to the background constant magnetic field $B_0 e_Z$. The magnetic field fluctuations

are described by the dimensionless functions $b_i(\mathbf{X}; Z)$, $i = (X, Y)$, taken to be Gaussian processes.

The configuration of the magnetic lines was studied in detail in previous papers, e.g. [1, 26]. The particles' guiding centers move along the field lines with a velocity that is a stochastic function; here, we will assume that the velocity along the main magnetic field is constant. We also assume that the unperturbed field is strong enough so that the motion of the particles can be described in the drift approximation. We consider that the electric field is negligible, so that the guiding center equations of motion take the form

$$\frac{dX}{dt} = \beta b_X(\mathbf{X}; Z) V_{\parallel} + V_{\text{dr}X}, \quad (2)$$

$$\frac{dY}{dt} = \beta b_Y(\mathbf{X}; Z) V_{\parallel} + V_{\text{dr}Y}, \quad (3)$$

$$\frac{dZ}{dt} = V_{\parallel}, \quad (4)$$

where V_{\parallel} is the component of the particle velocity parallel to the background magnetic field and \mathbf{V}_{dr} ($V_{\text{dr}X}$, $V_{\text{dr}Y}$) is the drift velocity which, for our stationary magnetic field, is given as

$$\mathbf{V}_{\text{dr}} \simeq \frac{1}{\Omega} \mathbf{n} \times [\mu \nabla B + V_{\parallel}^2 (\mathbf{n} \cdot \nabla) \mathbf{n}]. \quad (5)$$

In equation (5), $\Omega = eB/mc$ is the gyration frequency, $\mathbf{n} = \mathbf{B}/B$ is the unit vector along the field line, $\mu = V_{\perp}^2/2B$ is the magnetic moment and V_{\perp} is the component of the particle velocity perpendicular to the background magnetic field. The Z -component of the drift velocity is neglected, as well as the drift due to the time variation of the magnetic field (which is considered as stationary here). Two additional approximations can be introduced in equation (5), although they are not compulsory in developing the model. They considerably simplify DCT calculations without significantly affecting the results. Firstly, since the amplitude of the magnetic field fluctuations is very small, we can neglect the terms $[b_i(\mathbf{X}; Z)]^k$, $k > 2$, in the drift velocity and retain only the dominant, first-order, terms [25]:

$$V_{\text{dr}X} \simeq -\frac{V_{\parallel}^2}{\Omega} \frac{\partial b_Y[\mathbf{X}(Z); Z]}{\partial Z} \equiv -\frac{V_{\parallel}^2}{\Omega} b_{ZY}[\mathbf{X}(Z); Z], \quad (6)$$

$$V_{\text{dr}Y} \simeq \frac{V_{\parallel}^2}{\Omega} \frac{\partial b_X[\mathbf{X}(Z); Z]}{\partial Z} \equiv \frac{V_{\parallel}^2}{\Omega} b_{ZX}[\mathbf{X}(Z); Z], \quad (7)$$

where we have defined the vector \mathbf{b}_{Zj} [$j = X, Y$] as

$$\mathbf{b}_{Zj} \equiv \left(\frac{\partial b_X[\mathbf{X}(Z); Z]}{\partial Z}, \frac{\partial b_Y[\mathbf{X}(Z); Z]}{\partial Z} \right) \equiv (b_{ZX}[\mathbf{X}(Z); Z], b_{ZY}[\mathbf{X}(Z); Z]).$$

Secondly, the parallel velocity V_{\parallel} appearing in equation (4) is the particle velocity along the magnetic lines and is considered here to be constant and to equal the thermal velocity V_{th} . Thus, the drift velocity is a simple stochastic process that fluctuates due only to \mathbf{b} and its derivatives.

Equations (2) and (3) must be completed by specifying the statistical properties of the random quantities. For the description of the fluctuating magnetic field, we make an assumption about the statistical properties of the magnetic potential Ψ (i.e. the Z -component of the stochastic part of the vector potential) and then derive from it the statistical characteristics of the magnetic field and of its gradients. This procedure ensures the zero divergence condition for the fluctuating magnetic field to be fulfilled. Ψ is taken as a Gaussian random field,

spatially homogeneous (in the statistical sense) in the (X, Y) -plane, and stationary (again in the statistical sense). The Eulerian auto-correlation function is taken as [23]

$$M(\mathbf{X}; Z) = \langle \Psi(\mathbf{0}; 0) \Psi(\mathbf{X}; Z) \rangle = M_1(\mathbf{X}) M_2(Z), \quad (8)$$

where

$$M_1(\mathbf{X}) = \beta^2 B_0^2 \lambda_x^2 \exp\left(-\frac{X^2}{2\lambda_x^2}\right) \exp\left(-\frac{Y^2}{2\lambda_y^2}\right) \quad (9)$$

and

$$M_2(Z) = \exp\left(-\frac{Z^2}{2\lambda_z^2}\right), \quad (10)$$

where three characteristic correlation lengths are defined: the parallel correlation length λ_z and the perpendicular correlation lengths λ_x and λ_y . Note that we can define the vector potential with different normalization factors, such as $\lambda_x \lambda_y$, λ_x^2 or λ_y^2 . We have chosen the second case in order to keep the analysis close to the one in [33]. The qualitative results are not changed by the particular choice of the normalization factor. Dimensionless coordinates $\{\mathbf{x} = (x, y), z\}$ may then be defined by $x := X/\lambda_x$, $y := Y/\lambda_y$ and $z := Z/\lambda_z$, and we also define the magnetic dimensionless potential as $\psi = B_0^{-1} \beta^{-1} \lambda_x^{-1} \Psi$. Using these dimensionless quantities and the assumptions made above, the system given in equations (2)–(4) becomes

$$\begin{aligned} \frac{dx(z)}{dz} &= \Lambda K_m \left. \frac{\partial \psi(\mathbf{x}(z); z)}{\partial y} \right|_{\mathbf{x}=\mathbf{x}(z)} + K_{\text{dr}} \left. \frac{\partial}{\partial z} \left[\frac{\partial \psi(\mathbf{x}(z); z)}{\partial x} \right] \right|_{\mathbf{x}=\mathbf{x}(z)} \\ &\equiv v_x[\mathbf{x}(z); z] = K_m b_x(\mathbf{x}; z) - K_{\text{dr}} b_{zy}(\mathbf{x}; z), \end{aligned} \quad (11)$$

$$\begin{aligned} \frac{dy(z)}{dz} &= -\Lambda K_m \left. \frac{\partial \psi(\mathbf{x}(z); z)}{\partial x} \right|_{\mathbf{x}=\mathbf{x}(z)} + \Lambda^2 K_{\text{dr}} \left. \frac{\partial}{\partial z} \left[\frac{\partial \psi(\mathbf{x}(z); z)}{\partial y} \right] \right|_{\mathbf{x}=\mathbf{x}(z)} \\ &\equiv v_y[\mathbf{x}(z); z] = \Lambda K_m b_y(\mathbf{x}; z) + \Lambda K_{\text{dr}} b_{zx}(\mathbf{x}; z). \end{aligned} \quad (12)$$

The dimensionless quantities that appear in equations (11) and (12) are the magnetic Kubo number [23]

$$K_m = \beta \frac{\lambda_z}{\lambda_x}, \quad (13)$$

the stochastic anisotropy parameter

$$\Lambda = \frac{\lambda_x}{\lambda_y} \quad (14)$$

and the drift Kubo number

$$K_{\text{dr}} = \beta \frac{V_{\text{th}}}{\Omega \lambda_x}, \quad (15)$$

which in our case take values as characteristic for ions. β is the dimensionless amplitude of magnetic field fluctuations (considered here as relatively strong, i.e. $\beta \simeq 10^{-2}$, see [27]), V_{th} is the thermal velocity of the ions and Ω their Larmor frequency. In the comparison between the DCT method and the test-particle simulations, we will assume $\frac{V_{\text{th}}}{\Omega} \simeq 3 \times 10^{-1}$ m (Larmor radius for ions), $\lambda_x \simeq \lambda_y \simeq 10^{-2}$ m and $\lambda_z \simeq 1$ m, in order that the drift Kubo number is not very small. In this case, the following ratio holds:

$$\frac{K_{\text{dr}}}{K_m} = \frac{V_{\text{th}}}{\Omega \lambda_z} \simeq 0.3, \quad (16)$$

and it follows that the second terms in equations (11) and (12) are not negligibly small (there is one order of magnitude difference between the two Kubo numbers).

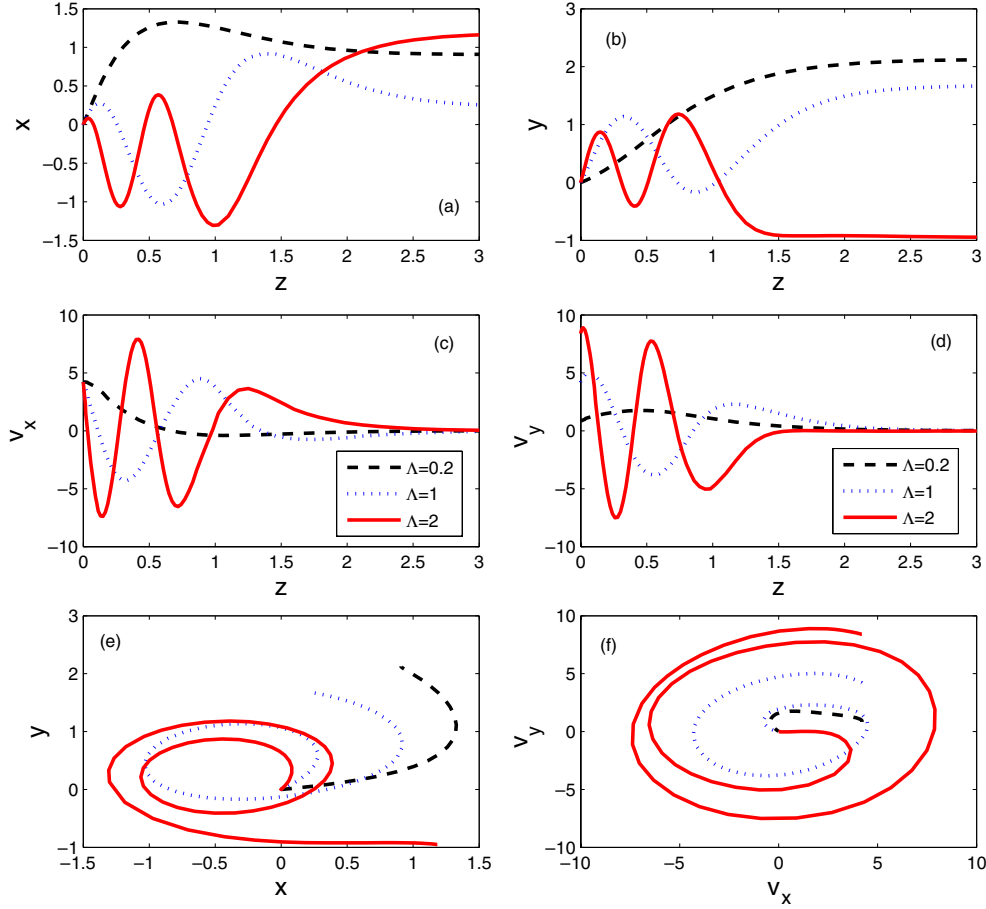


Figure 1. In (a) and (b) the solutions $x(z)$ and $y(z)$ of equations (11) and (12) are shown, in (c) and (d) the fluctuating velocities, in (e) the decorrelation trajectory and in (f) the hodograph, for the subensemble: $\psi^0 = 3$, $b_x^0 = b_y^0 = 2$, $b_{zx}^0 = 1$, $b_{zy}^0 = -1$, $K_m = 2$ and $K_{dr} = 0.2$.

3. Diffusion coefficients—the DCT approach

An extensive explanation of the DCT method can be found in the book of Balescu [2], and details of the explicit calculations are given in the appendix. Also, in order to apply the semi-analytical formalism specific to the DCT method, we have developed a code based on [28].

In figure 1, we show the solutions of the system (11)–(12) in the subplots (a) and (b), the velocities in (c) and (d), the trajectories in (e) and the hodograph in (f), for the subensemble $S \equiv \{\psi^0 = 3, b_x^0 = b_y^0 = 2, b_{zx}^0 = 1, b_{zy}^0 = -1\}$, for a fixed level of magnetic turbulence $K_m = 2$, for the drift ion Kubo number $K_{dr} = 0.2$ and for three values of the anisotropy parameter $\Lambda = \{0.2, 1, 2\}$ (the superscript 0 is related to the definition of the subensemble S , see the appendix, equation (A.2)). The solid line corresponds to $\Lambda = 2$, the dotted line to $\Lambda = 1$ and the dashed one to $\Lambda = 0.2$. From figures 1(a) and (b) it can be seen that the general shape of the solutions exhibits a few oscillations before stopping practically for $z \geq 3$ for all values of the anisotropy parameter. The number of oscillations increases with an increase in the anisotropy parameter Λ . For $\Lambda = 0.2$ there is no real oscillation.

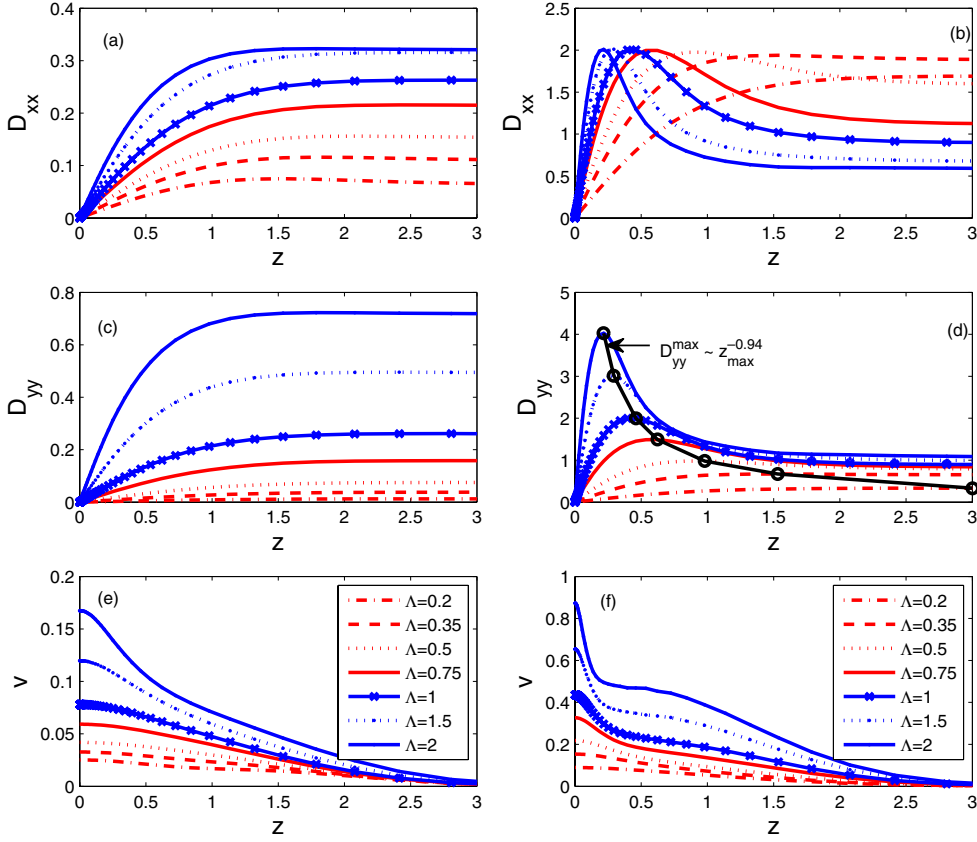


Figure 2. Running diffusion coefficients and the total velocities (the entire right-hand sides of equations (11) and (12)) for a fixed value of the drift Kubo number $K_{\text{dr}} = 0.2$, different values of the anisotropy parameter Λ , and $K_m = 0.5$ ((a), (c) and (e)) and $K_m = 3$ ((b), (d) and (f)).

The fluctuating velocities (see figures 1(c) and (d)) have practically the same shape as the solutions $x(z)$, $y(z)$, with oscillations present for $\Lambda \geq 1$. These oscillations are equivalent to decorrelation trajectories that are closed for $\Lambda \geq 1$ and open for $\Lambda \leq 1$. Because the Lagrangian field correlation has been damped out by the factor $\exp(-\frac{z^2}{2})$ for large values of z , $x^S(z) \simeq x^S$. These remarks are not general concerning the behavior of the particles but are specific to the particular subensemble. Important to note is that the *open trajectories* give the most substantial contribution to the value of *diffusion coefficients*.

In figure 2, we show the running diagonal diffusion coefficients for different values of the anisotropy parameter, a fixed value of the drift Kubo number $K_{\text{dr}} = 0.2$ (for all the subplots), and two values of the magnetic Kubo number $K_m = 0.5$ (all left subplots) and $K_m = 3$ (all right subplots). For $K_m = 0.5$, no trapping effect is present for both diffusion coefficients. The asymptotic values of the diffusion coefficients increase when the anisotropy parameter Λ increases, and the asymptotic regime is practically reached for $z \geq 3$ for all values of the anisotropy parameter. The running diffusion coefficients start with a linearly increasing part, corresponding to a ballistic regime, followed by the asymptotic (constant) regime. The total velocity decreases in all cases and tends to zero for $z \geq 3$. For $K_m = 3$, the behavior of the radial and poloidal running diffusion coefficients is different, as shown in figures 2(b) and (d).

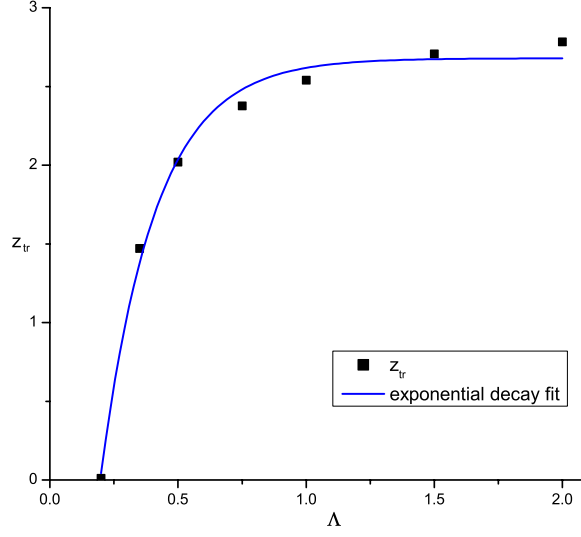


Figure 3. Trapping time interval z_{tr} as a function of the anisotropy parameter Λ , for $K_m = 3$ and $K_{dr} = 0.2$.

The diffusion coefficients reach a maximum followed by a decay, which is a signature of the trapping effect that is present for both $D_{xx}(z)$ and $D_{yy}(z)$. As the trapping effect is only present for $K_m = 3$, it follows that an increase in the level of magnetic turbulence favors trapping effects. This is visible for the radial diffusion coefficient (figure 2(b)) for $\Lambda \geq 0.5$, and it becomes more pronounced if the stochastic anisotropy parameter Λ increases.

The maximum values reached by the radial diffusion coefficients are practically the same, $D_{xx}^{max} \simeq 2$, for all stochastic anisotropy parameters Λ , as can be seen from figure 2(b). The maxima of the poloidal diffusion coefficients vary and are different from D_{xx}^{max} (see figure 2(d)), where, for different locations z_{max} of the maxima, different maximum values of the poloidal diffusion coefficient, $D_{yy}^{max}(z_{max})$, are reached, and actually the following scaling holds:

$$D_{yy}^{max}(z_{max}) = 0.96(z_{max})^{-0.94}.$$

A decrease in the values of the maxima is observed if the anisotropy parameter decreases. The *trapping time interval* is defined as $z_{tr} \equiv z_{as} - z_{max}$, where z_{as} is the starting point of the asymptotic regime. The difference between the maximum value and the asymptotic one for the poloidal diffusion coefficients is $\Delta_{yy} \equiv D_{yy}^{max} - D_{yy}^{as}$ and it depends on z_{tr} as

$$\Delta_{yy} = 0.0016 \exp(2.5352 z_{tr}).$$

It also follows that *the trapping time interval* z_{tr} is larger, the larger the anisotropy parameter is; e.g. for $\Lambda = 2$, $z_{tr} \simeq 2.75$, and for $\Lambda = 0.35$, $z_{tr} \simeq 1.5$. The trapping interval z_{tr} is shown as a function of Λ for $K_m = 3$ and $K_{dr} = 0.2$ in figure 3, and an exponential fit reveals the following dependence of z_{tr} on Λ :

$$z_{tr}(\Lambda) = 2.67891 - 6.76281 \exp(-\Lambda/0.21236).$$

The *trapping time interval* increases for $\Lambda \leq 1$ faster than in the case $\Lambda \geq 1$, and a kind of stabilization of the growth of z_{tr} appears for $\Lambda \geq 1.5$ in the case of the specific Kubo numbers chosen.

Figure 4 shows the dimensionless running diffusion coefficients for isotropic stochastic fields and for different values of the drift Kubo number. As before, trapping effects are

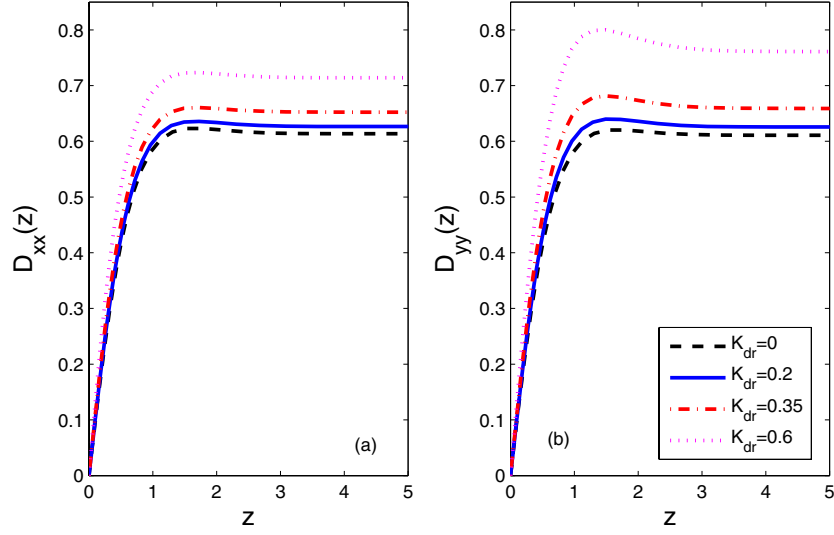


Figure 4. Running diffusion coefficients for a fixed value of the magnetic Kubo number $K_m = 1.0$, isotropic perturbations ($\Lambda = 1.0$) and for different values of the drift Kubo number K_{dr} .

basically absent for the relatively low value of $K_m = 1$, and the asymptotic values of the diffusion coefficients show a relatively weak dependence on the drift Kubo number K_{dr} .

So far, we have considered cases with K_{dr} varying up to relatively large values, with the aim to have a parametric study of the DCT method that can be tested and compared with test-particle simulations (see section 4.3.1). Values of K_{dr} of the order of 0.3 are realized under conditions of astrophysical plasmas, e.g. in the Solar corona, whereas in confinement devices K_{dr} is much smaller. For instance, in a tokamak such as ITER, a typical impurity like Be^{4+} will have $K_{dr} \approx 0.0022$ (see section 4.3.2 for more details). For the latter value of K_{dr} , figure 5 shows the dimensionless and the dimensional running diffusion coefficients for different values of the anisotropy parameter Λ , as yielded by the DCT method. These results will be discussed below in section 4.3.2, together with the respective results from the test-particle simulations. Note that in figure 5 the scaling of the asymptotic diffusion coefficients with Λ inverses when going from dimensionless to dimensional units, which will be explained in section 4.3.1 (equations (20), and (21)).

4. Diffusion coefficients—test-particle simulation

In order to solve the system of equations (11)–(12) numerically, we first generate the stochastic magnetic field components b_x , b_y , together with the constant background component b_z , with prescribed auto-correlation functions on a three-dimensional grid. Test particles are then traced in this environment by interpolating the stochastic fields in between the grid sites.

4.1. Generation of the stochastic fields

To generate the vector potential $A_Z \equiv \Psi$ on a three-dimensional grid, we use numerical Fourier transform methods and make use of the Wiener–Khinchine theorem. We first Fourier transform the spatial auto-correlation $M(\mathbf{X}; Z)$ of A_Z (equations (8), (9) and (10)), which

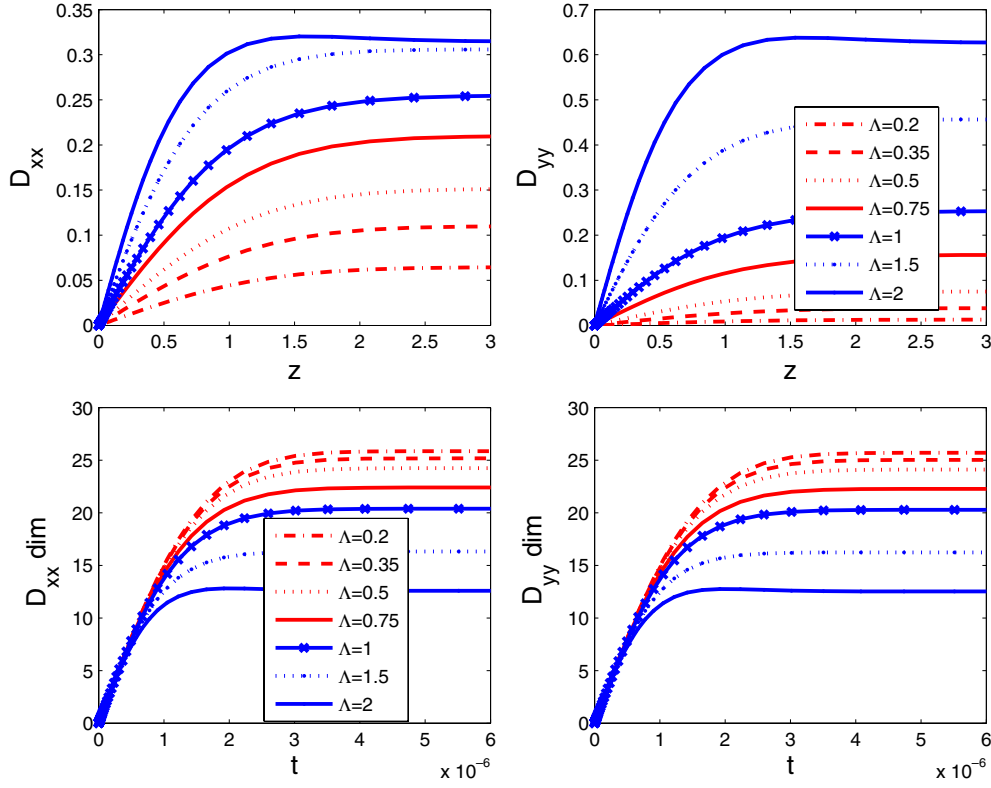


Figure 5. Running diffusion coefficients for different values of the anisotropy parameter Λ , and for $K_m = 0.5$, $K_{dr} = 0.0022$; the two top panels show the dimensionless coefficients and the two bottom panels show the dimensional ones.

yields $\widehat{M}(k_X, k_Y, k_Z)$, and the Fourier transform \widehat{A}_Z of A_Z is then given as

$$\widehat{A}_Z = |\widehat{M}(k_X, k_Y, k_Z)|^{1/2} \exp(i\phi_{K_X, K_Y, K_Z}) \quad (17)$$

with the phases ϕ_{K_X, K_Y, K_Z} chosen uniformly random in $[0, 2\pi]$, and from which A_Z is determined by Fourier back-transformation. The derivatives of A_Z are also calculated via Fourier space transformation, e.g. $\partial_X A_Z$ is calculated as the Fourier back-transform of $\partial_X \widehat{A}_Z = iK_X \widehat{A}_Z$, and likewise for the other or higher order derivatives.

In this way, the magnetic field components

$$(b_X(m, j, k), b_Y(m, j, k)) = (\partial_Y A_Z(m, j, k), -\partial_X A_Z(m, j, k))$$

and their derivatives with respect to Z , as needed in equations (11)–(12), are determined on a three-dimensional grid, $1 \leq m, j, k \leq N$. We use natural dimensional coordinates (X, Y, Z) in the construction of the grid so that $b_x(\mathbf{x}; z) = b_X(\lambda_x x, \lambda_y y, \lambda_z z)$.

The magnetic field components obey Gaussian distributions, as a consequence of the central limit theorem, and their standard deviations, σ_{b_x} and σ_{b_y} , are enforced to be equal to one. Figure 6 shows different representations of the magnetic field. By construction, the magnetic field is periodic in all three directions, and particles leaving the simulation box are re-injected at the plane opposite to the one through which they leave.

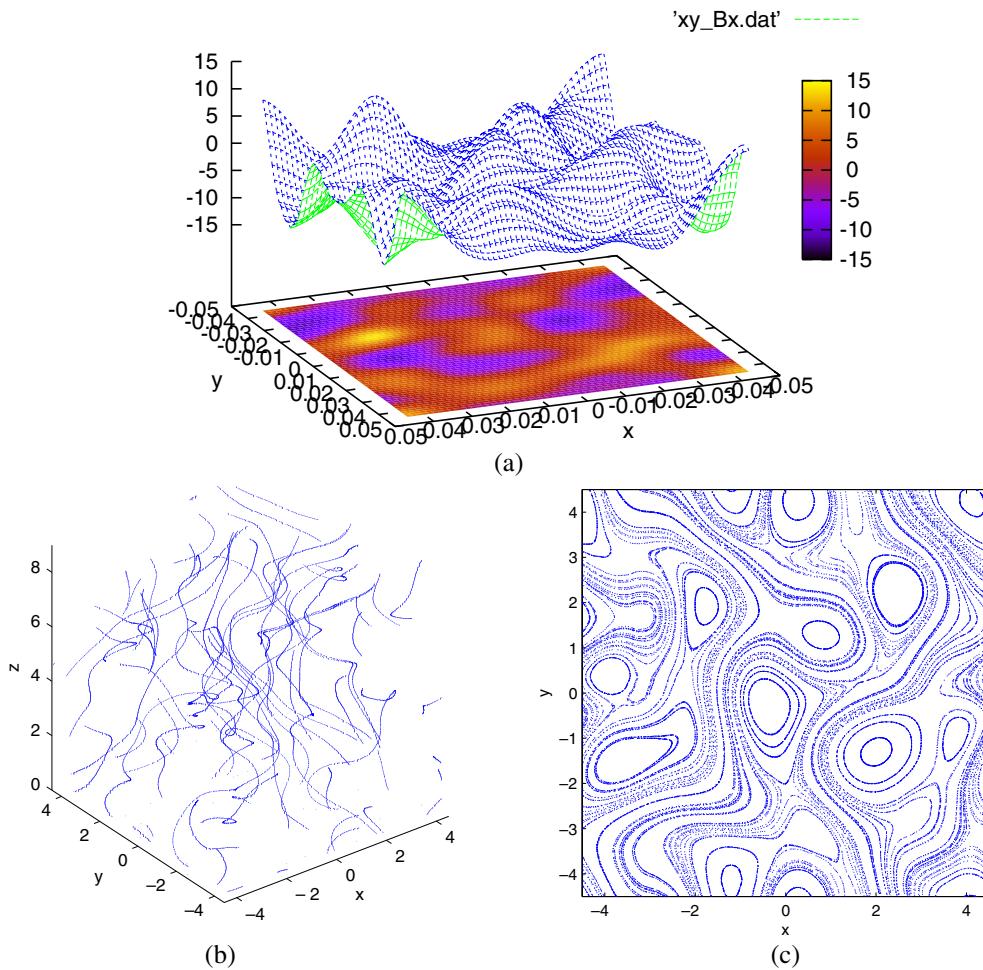


Figure 6. Shown are (a) the fluctuating magnetic field component b_x as a function of x and y for fixed z , (b) field lines in three-dimensional space and (c) field lines projected onto the x - y -plane for $z = \text{const}$.

4.2. Integration of the equation

The system of equations (11)–(12) is numerically integrated with a fourth-order Runge–Kutta, adaptive step-size scheme. The values of $b_x(X, Y, Z)$ and $b_y(X, Y, Z)$ for points (X, Y, Z) in between the grid sites are calculated by interpolating between the magnetic field components of the nearest grid sites with third-order splines, following the method in [29].

The grid size in each direction is such that it contains several correlation lengths. The stochastic magnetic field is generated on a grid with 64^3 grid points in most cases, and exceptionally also with 128^3 grid points, with a grid spacing such that the number of correlation lengths λ_i in each direction is 9–11 per 64 grid points. The latter was found to be an optimum choice for having (1) good resolution of the basic magnetic field structures (in Fourier as well as in position space), (2) many correlation lengths in the domain so that the particles do experience the effect of the correlations and (3) to have a grid size that is still manageable computationally.

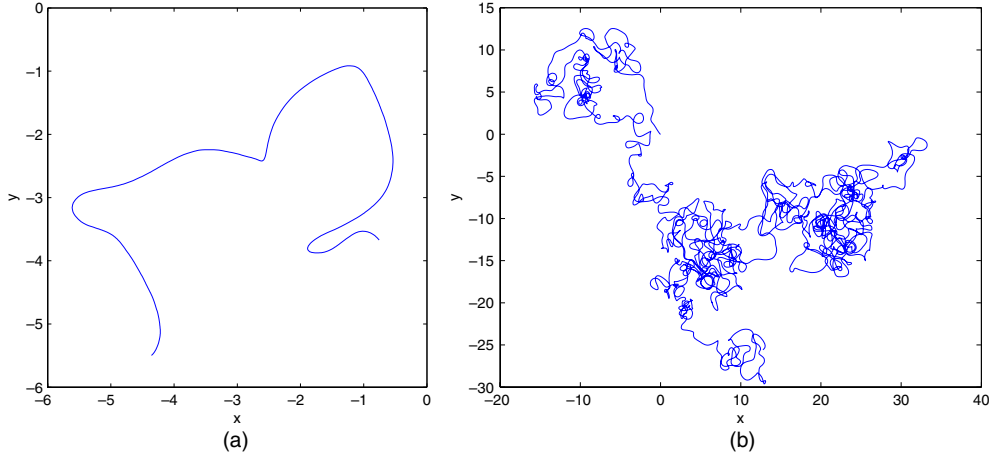


Figure 7. A typical particle trajectory, projected onto the x - y -plane, for a short (a) and a longer (b) integration time.

The running diffusion coefficients for the motion of the ions in the magnetic field are determined as

$$D_{xx}(z) = \frac{\langle [x(z) - x(0)]^2 \rangle}{2z} \quad (18)$$

and

$$D_{yy}(z) = \frac{\langle [y(z) - y(0)]^2 \rangle}{2z} \quad (19)$$

where the averaging is taken over 10^6 test particles in 10^3 different realizations of stochastic magnetic fields.

4.3. Results

4.3.1. Comparison with the DCT method. We consider ion diffusion in the same magneto-static, perturbed magnetic field environment to which we applied the DCT method in section 3. The parameter values we use are $\lambda_x = 10^{-2}$ m and $\lambda_z = 1$ m for the correlation lengths (see text after equation (15)), and K_m , Λ and K_{dr} are free parameters that are varied, whereby the strength of the magnetic perturbations is kept to the order of $\beta \sim 10^{-2}$, and the Larmor radius is varied around $\frac{V_{th}}{\Omega} \sim 3 \times 10^{-1}$ m. Figure 7 shows a typical example of a trajectory.

Figures 8(a) and (b) show the dimensionless radial $D_{xx}(z)$ and poloidal $D_{yy}(z)$ diffusion coefficients for different values of the drift Kubo number K_{dr} and for fixed values of the magnetic Kubo number ($K_m = 1$) in the isotropic case ($\Lambda = 1$). Diffusion always is of normal nature (in the sense that the mean square displacement scales linearly with time, and an asymptotic regime in the diffusivities is reached). The decrease in the diffusivities with increasing K_{dr} in figure 8(c) actually holds only in dimensionless units. In physical units, we have for the diffusion coefficient D_{XX} in the X -direction

$$D_{XX} = \frac{V_{th} \lambda_x^2}{\lambda_z} D_{xx}, \quad (20)$$

so that there is an increase in D_{XX} with increasing K_{dr} , and the same is true for D_{YY} . The diffusive process thus speeds up with increasing Larmor radius, i.e. with increasing

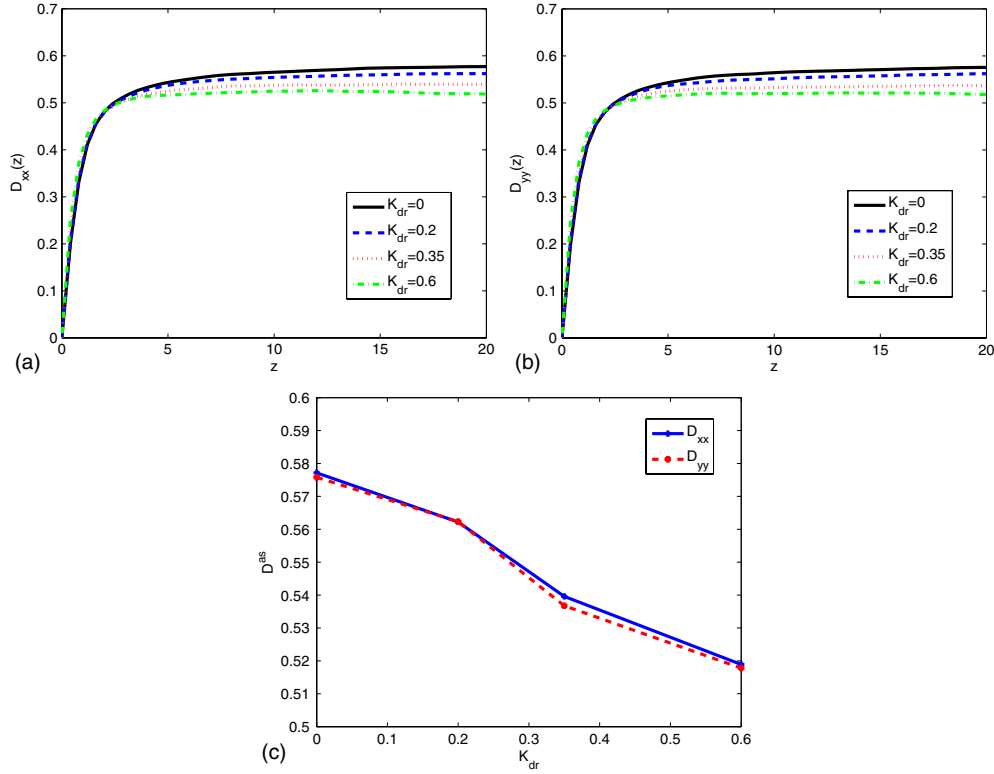


Figure 8. Radial (a) and poloidal (b) running diffusion coefficients for $K_m = 1$, stochastic isotropy ($\Lambda = 1$) and for different values of the drift Kubo number K_{dr} . (c) Asymptotic values of the diffusion coefficients as a function of K_{dr} , for $K_m = 1$ and $\Lambda = 1$.

thermal velocity (temperature) for a given ion species, or with increasing ion mass for a given temperature.

Regarding the comparison with the DCT method (figure 4), the values of the diffusion coefficients coincide within 20% with the results yielded by the DCT method, we find though a different scaling of the diffusion coefficient with the drift Kubo number.

For fixed drift Kubo number ($K_{dr} = 0.2$) and for two different magnetic Kubo numbers, figures 9(a)–(d) show the radial $D_{xx}(z)$ and the poloidal $D_{yy}(z)$ diffusion coefficients for different degrees of anisotropy Λ (throughout, we fix the value of $\lambda_x = 10^{-2}$, and we set $\lambda_y = \lambda_x/\Lambda$, and K_m is changed by changing the intensity of the magnetic perturbation β). Basically, D_{xx} decreases and D_{yy} increases with increasing Λ , whereby this effect is more pronounced the larger the K_m is, i.e. the stronger the magnetic perturbation is. Again although, for the diffusion coefficient D_{YY} in physical units

$$D_{YY} = \frac{V_{th}\lambda_y^2}{\lambda_z} D_{yy} = \frac{V_{th}\lambda_x^2}{\Lambda^2\lambda_z} D_{yy}, \quad (21)$$

the opposite is true, D_{YY} decreases with increasing Λ , as does D_{XX} . The asymptotic values of radial and poloidal diffusion coefficients are shown as functions of Λ in figure 9(e) for $K_{dr} = 0.2$.

Comparing again with the results from the DCT method in figure 2, we see that the values of the diffusion coefficients coincide within 20% for D_{yy} in the case $K_m = 0.5$ and for D_{xx} in the case $K_m = 3.0$, and they also exhibit the same scaling with Λ . For D_{yy} in the case

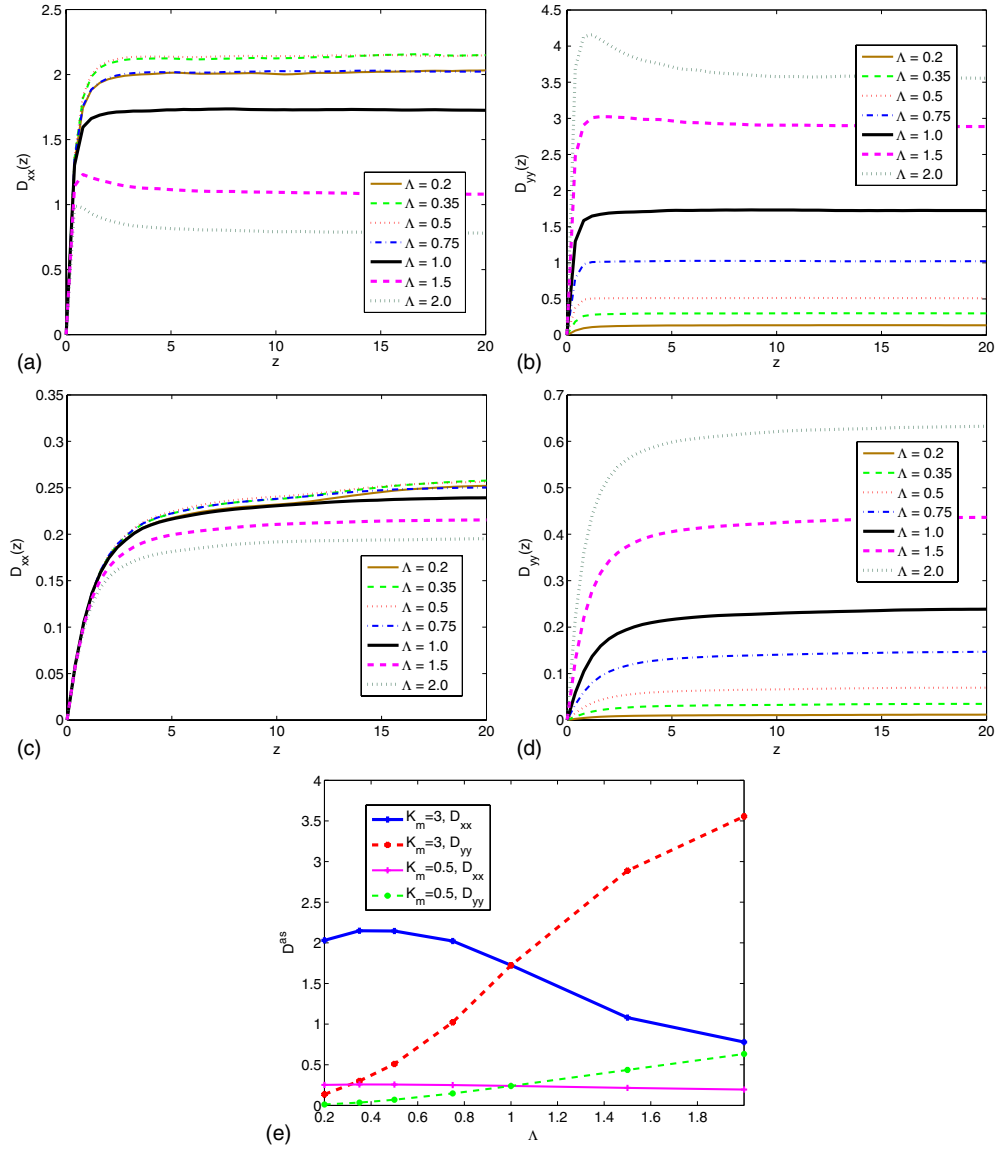


Figure 9. Radial (a), (c) and poloidal (b), (d) running diffusion coefficients for $K_{dr} = 0.2$, $K_m = 3$ (a), (b), $K_m = 0.5$ (c), (d), and for different values of the stochastic isotropy parameter Λ . (e) Asymptotic values of the diffusion coefficients as a function of Λ , for $K_{dr} = 0.2$ and two different values of K_m (0.5 and 3).

$K_m = 3.0$ the scaling with Λ is the same, the differences in values reach though now 50%, as for D_{xx} in the case $K_m = 0.5$, where moreover the scaling with Λ is different. In basically all cases shown so far, the time needed to reach the asymptotic state in the test-particle simulations is roughly 5 times larger than in the DCT method.

4.3.2. Impurities in ITER-like conditions. We now turn to impurities in ITER-like conditions, i.e. we assume an ion temperature $T_i = 8.1$ keV and a background magnetic field $B_0 = 5.3$ T.

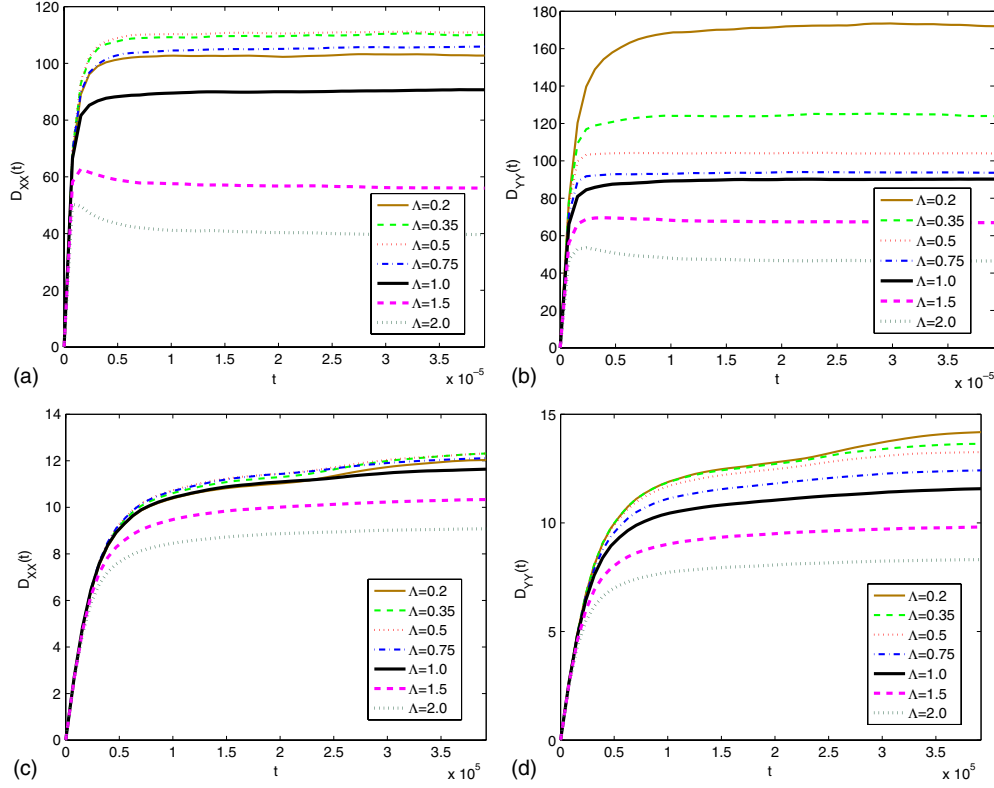


Figure 10. Be^{4+} (physical units ($\text{m}^2 \text{s}^{-1}$)): Radial (a), (c) and poloidal (b), (d) running diffusion coefficients for $K_m = 3$ (a), (b), $K_m = 0.5$ (c), (d), and for different values of the stochastic anisotropy parameter Λ .

The ions we consider are He^{2+} and the impurities Be^{4+} , Ne^{10+} and W^{74+} , as they are relevant for tokamak devices of the ITER type. With the temperature and magnetic field given, the drift Kubo number is fixed for each ion species and is not a free parameter anymore. We thus vary, in the following, only K_m (i.e. β) and Λ .

The magnetic field environment is as before, though from now on we show all the results in physical units. This concerns also the time scale. According to equation (4), in which $V_{||} = V_{th}$ is assumed and which is integrated analytically, we have $t = Z/V_{th} = \lambda_z z/V_{th}$, so that the time scale depends on the ion mass.

Figures 10(a)–(d) show the results for the running diffusion coefficients of Be^{4+} , for different values of Λ and K_m . In all cases, an asymptotic, normal diffusive regime is reached. The case $K_m = 0.5$ (figures 10(c) and (d)) is also treated with the DCT method, see figure 5. The two methods agree within a factor of 2 for Λ small, and coincidence becomes better with increasing Λ . The results, together with those for He^{2+} , Ne^{10+} and W^{74+} , are summarized in figures 11(a)–(d), where the values of the asymptotic diffusion coefficients are shown as a function of the atomic number Z_i . The diffusion coefficients (i) decrease with increasing atomic number, as a direct consequence of the increasing mass and thus decreasing thermal velocity. The drift Kubo numbers are relatively small and of similar magnitude ($K_{dr}^{\text{He}^{2+}} = 0.0030$, $K_{dr}^{\text{Be}^{4+}} = 0.0022$, $K_{dr}^{\text{Ne}^{10+}} = 0.0013$ and $K_{dr}^{\text{W}^{74+}} = 0.0005$), so that from the results in figures 8(a)–(c) we expect very close values of the normalized

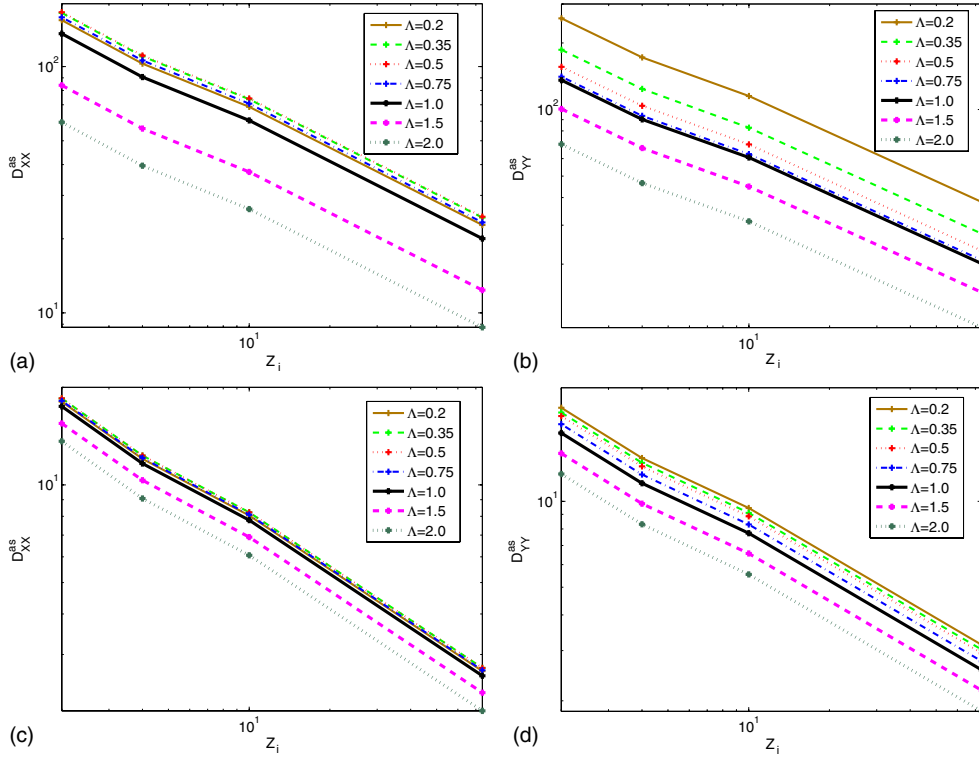


Figure 11. He^{2+} , Be^{4+} , Ne^{10+} and W^{74+} (physical units ($\text{m}^2 \text{s}^{-1}$)): Radial (a), (c) and poloidal (b), (d) asymptotic diffusion coefficients for $K_m = 3$ (a), (b), $K_m = 0.5$ (c), (d), and for different values of the stochastic anisotropy parameter Λ , as a function of the atomic number Z .

perpendicular diffusion coefficients, and it is actually the motion in the Z -direction that leads to the differences in the dimensional diffusivities, since, as mentioned, $t = Z/V_{\text{th}} \propto \sqrt{m Z_i}$. Moreover, (ii) the diffusion coefficients decrease with increasing Λ , and (iii) they increase with increasing K_m , i.e. increasing amplitude of the magnetic perturbation. All three findings are in accordance with section 4.3.1.

4.3.3. Lorentz force and toroidal geometry. The aim of this section is to investigate as to how far some of the assumptions we made influence the results. We again consider ITER-like conditions and choose He^{2+} as test particles, K_{dr} is thus again fixed, and we concentrate on the isotropic case ($\Lambda = 1$), with a level of stochastic perturbation $\beta = 10^{-2}$.

First, we investigate how accurate the linearized gyro-center approximation of equations (11) and (12) is. Thereto, we integrate the equations of motions in terms of the Lorentz force,

$$\begin{aligned} \frac{d\mathbf{V}(t)}{dt} &= \frac{q}{m} \mathbf{V} \times \mathbf{B}, \\ \frac{d\mathbf{X}(t)}{dt} &= \mathbf{V} \end{aligned} \quad (22)$$

with q the particle charge. The two perpendicular components of initial velocity, $V_X(0)$ and $V_Y(0)$, are chosen random with Gaussian distribution that corresponds to the temperature

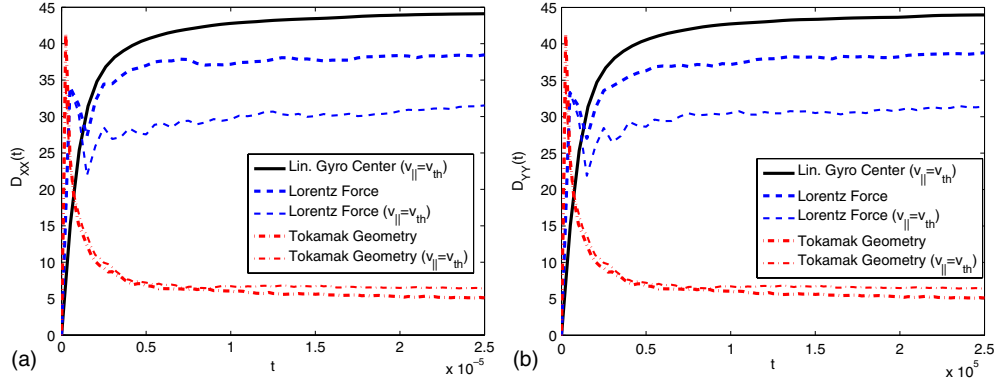


Figure 12. He^{2+} (physical units ($\text{m}^2 \text{s}^{-1}$)): Radial (a) and poloidal (b) running diffusion coefficients for $\beta = 10^{-2}$ and $\Lambda = 1$, in cylindrical and toroidal geometry, and with the gyro-center approximation compared with the integration of the Lorentz force.

T_i , and the parallel component $V_Z(0)$ is either random and Gaussian distributed (again with temperature T_i), or we let it equal $V_{\text{th}} \equiv \sqrt{\frac{3k_B T_i}{m_{\text{He}}}}$, as in the gyro-center approximation.

Figures 12(a) and (b) show the corresponding running diffusion coefficients. With $V_Z(0) = V_{\text{th}}$, the gyro-center approximation overestimates the diffusivity by roughly 50%, it is though closer to the case with random $V_Z(0)$, still overestimating it now by 15%. These differences must be attributed to the linearity of the gyro-center approximation; finite ion Larmor radius effects may also be present but must be expected to be less important since the Larmor radius of He^{2+} is 1.7×10^{-3} m, i.e. one-fifth of the perpendicular correlation length λ_x .

Second, we address the question of how far the effects of toroidal geometry and shear alter the results presented so far. Thereto, we use the standard (vacuum) tokamak magnetic field

$$\mathbf{B} = \frac{R_0 B_0}{R_0 + r \cos \theta} \left(\hat{e}_\phi + \frac{r}{R_0 q(r)} \hat{e}_\theta \right) \quad (23)$$

(see [30]) with safety factor

$$q(r) = \frac{(\nu + 1)\xi}{1 - (1 - \xi)^{\nu+1}}, \quad \xi = r^2/a^2 \quad (24)$$

(see [31]), with major radius $R_0 = 6.2$ m and minor radius $a = 2$ m, and where $q(0) = 1$, $q(a)/q(0) = \nu + 1$, and we arbitrarily choose $\nu = 2$. (r, θ, ϕ) are toroidal coordinates, r is the radial coordinate along the minor radius, θ the poloidal angle and ϕ the toroidal angle. Onto the background field we superpose the stochastic magnetic field (with $\beta = 10^{-2}$) that is numerically generated as before on a 3D Cartesian grid. In order to transform the fields to toroidal geometry, the Cartesian grid is stretched in the z ($=\phi$)-direction, shifted so that its center coincides with $r = 0$, and bent to a ring embedded in three-dimensional space by applying a transformation from Cartesian to polar coordinates in the perpendicular direction,

$$\begin{aligned} b_r &= b_x \cos \theta + b_y \sin \theta, \\ b_\theta &= -b_x \sin \theta + b_y \cos \theta. \end{aligned}$$

Due to the bending, the correlation lengths at the low- and high-field sides are slightly different, but this can be expected to be of minor importance for our purpose here.

Figures 12(a) and (b) show two cases of integrating the Lorentz force in toroidal geometry, one with random $V_{\parallel}(0)$ and one with $V_{\parallel}(0) = V_{\text{th}}$ (with V_{\parallel} in toroidal geometry corresponding to V_Z in cylindrical geometry), respectively (no drift approximation is applied). They yield

very similar results; the assumption $V_{\parallel} = V_{\text{th}}$ is more appropriate in toroidal than in cylindrical geometry, the diffusivities are though roughly 7 times smaller than those derived in cylindrical geometry (see the discussion in section 5.3).

5. Summary and conclusion

5.1. The DCT method

The problem of ion diffusion in a stochastic magnetic field was treated by starting from the Langevin equations in the linearized guiding center approximation. Since the Corrsin approximation ignores the trapping effect, which necessarily exists in a relatively strong turbulent plasma, the method of decorrelation trajectories was applied. In this paper, we studied the influence of the magnetic Kubo number, the drift Kubo number and stochastic anisotropy on the diffusion of ions, with intended application of impurity transport in plasma confinement devices. The model together with the main elements of the decorrelation trajectory method was established in sections 2 and 3.

We have shown that the stochastic drifts provide a decorrelation mechanism of the particles from the magnetic field lines. Subdiffusive behavior of the particles is not observed and the particles diffuse even in the absence of perpendicular collisional diffusion.

In section 3, we have shown deterministic decorrelation trajectories for fixed values of K_m and K_{dr} and different values of the anisotropy parameter Λ , in order to investigate the influence of the latter on the shape of the trajectories. An increased value of Λ causes oscillations around the starting point in a given subensemble, and the trapping effect is more pronounced, the larger Λ and K_m are. This is also obvious from the graphical representation of the running diffusion coefficients, which provides an interesting insight into the transient behavior of the diffusive process. The diagonal coefficients start with a linear part, indicating a ballistic regime, which is followed by a trapping regime, whereafter the saturated asymptotic value is reached (although there is no distinct feature of the trapping regime in the running diffusion coefficients from the test-particle simulations, trapping effects are visible only in representations of trajectories, see figure 7(b)). The stochastic magnetic drift has practically the same influence on the ions' diffusion as has the magnetic shear on the intrinsic diffusion of magnetic field lines.

Finally we note that the time for reaching the asymptotic regime, typically $t \simeq 10^{-5}$ s, is equivalent to $z \simeq 3$ m for $V_{\text{th}} \simeq 10^5$ m s $^{-1}$, which is close to the correlation length in the Z-direction, as used in the calculations.

5.2. Test-particle simulations

In section 4, we repeated the calculation of the diffusion coefficients by performing test-particle simulations, using the same drift approximation as in the DCT method and applying the same values of K_m , K_{dr} and Λ . No trapping effect is present in these cases for both diffusion coefficients. The simulations and the DCT method yield diffusion coefficients that differ by 50% or less, they can thus be considered to be in good qualitative agreement. Another instance where the results obtained by the DCT method were compared with numerical test-particle simulation, and where also relatively good agreement was found, is given in [33, 34].

In order to investigate the appropriateness of the linear guiding center approximation, we let the particles obey the Lorentz force, and it turned out that the linear gyro-center approach overestimates the diffusivities by 50% (figures 12(a) and (b)), non-linearities and possibly also finite Larmor radius effects are thus important for a quantitatively correct determination of the diffusion coefficients.

In the last step, we investigated the importance of the effects of toroidal geometry and shear by integrating the Lorentz force in an ITER-like toroidal geometry that was slightly perturbed, which yields diffusion coefficients that are 7–8 times smaller than those found in cylindrical geometry (figures 12(a) and (b)), geometric and shear effects are thus important, as expected. As mentioned, trapping is not present in the linearized gyro-centre approximation, it appears though in the Lorentz force approach.

5.3. Discussion

The differences between the results of the DCT method and the test-particle simulations must be attributed to the assumptions made in the semi-analytical DCT method, since in the test-particle simulations we did not make any further assumptions beyond those made in the initial equations and field environment, so the latter must be considered to yield more trustworthy results than the DCT method and it can indeed be used to assess the DCT method.

Collisions were not taken into account, neither in the DCT approach, nor in the test-particle simulations. The equations of motions are solved for a time such that an asymptotic regime in the diffusivities is reached, which is of the order of 3×10^{-5} s. For the four impurity species we consider, and with the assumed plasma parameters, the collision frequencies are 2×10^2 (He²⁺), 6×10^2 (Be⁴⁺), 2×10^3 (Ne¹⁰⁺), and 4×10^4 (W⁷⁴⁺) s⁻¹. This implies that, for the time interval considered, all the investigated impurities are not affected by collisions, a much longer integration time would have to be used in order to reach the collisional regime, which, from the side of the test-particle simulations, would become very demanding on computation time for the light ions. We also note that it is, in principle, possible to include collisions in the DCT formalism, as done, e.g., in [32].

The comparison of the DCT method with the test-particle simulations was done in slab geometry without magnetic shear. In order to validate this set-up in its potential for being predictive for tokamaks such as ITER, a more realistic toroidal topology was used in section 4.3.3, which, in contrast to the slab geometry, (1) has a realistic poloidal background magnetic field and (2) exhibits shear ($s = r\partial_r q/q \neq 0$) (see equations (23) and (24)), with a realistic safety factor profile. The magnetic field is again perturbed with a reasonable level of fluctuating fields that are correlated in space, as expected for turbulent fields (e.g. zonal flows and streamers). From this set-up, it follows that the toroidal topology exhibits much better confinement properties than the slab geometry, which is reflected in the diffusivities being lower than in the case of slab geometry (see section 4.3.3 and figure 12).

The DCT method has not yet been applied to particles in a toroidal and sheared topology, in [23, 33] though, the diffusion of magnetic field lines has been studied in sheared topologies with the DCT method, and it is possible to extend this analysis to particles.

After all, our study implies that for the DCT method to yield quantitatively meaningful results, (1) a higher order, non-linear guiding center approach, (2) a toroidal geometry with (3) a poloidal field and (4) shear must be used, since only under these conditions we find very good coincidence of the test-particle simulations with experimental results from current tokamaks, which we present in section 5.4.

What has not been done in this study and should be addressed in future work is a long-term study of the system that includes collisions, and the effects of turbulent electric fields. Also, the turbulent electromagnetic fields would be more realistic if they were taken from MHD simulations, which is directly feasible with test-particle simulations; for the DCT method it first would have to be worked out.

5.4. Conclusion

With the above-mentioned restrictions in mind, our results on impurity transport can be summarized as follows (see figures 11(a)–(d)):

- (i) In the stochastic magneto-static environment considered, diffusion is always of normal nature;
- (ii) the diffusivities increase with increasing level of turbulence;
- (iii) the diffusivities of the impurities scale as $m_{Z_i}^{-1/2}$ with the ion mass; and
- (iv) anisotropy in the turbulent magnetic field alters the diffusivities.

The theoretical, neoclassical values for the diffusion coefficients are smaller than unity, of the order $0.5 \text{ m}^2 \text{ s}^{-1}$, whereas in experiments much larger, anomalous values are found. For example, [6] reports a diffusion coefficient $D \approx 4 \text{ m}^2 \text{ s}^{-1}$ from the combined analysis of supersonic and stationary injections; a maximum value of $4.5 \text{ m}^2 \text{ s}^{-1}$ for the diffusion coefficient of Ne^{10+} was found in [5] for the edge region, and similar results are presented in [18]. These numerical values are in agreement with our results for slab geometry (see figures 11(c) and (d)), for relatively weak magnetic turbulence ($K_m = 0.5$) and a stochastic anisotropy parameter $\Lambda = 2$, and they are in good agreement with the values we find in sheared toroidal geometry when tracking the particles with the Lorentz force (test-particle simulations, figures 12(a) and (b)) (where we lack though a parametric study). Finally, the decrease in the diffusion coefficients with increasing atomic number Z for all the impurities (figures 11(c) and (d)) was also observed in [18] for the core region.

After all, the DCT method and the linear guiding center approximation, together with the magnetic slab topology used, are able to give useful qualitative information about the diffusion of impurities, and it can be expected that further development of the DCT model (with the use of sheared toroidal instead of slab geometry, a non-linear guiding center description, and with the inclusion of the electric field) would lead to a realistic and fully quantitative model.

Acknowledgments

This work, supported by the European Commission under the contract of Association between EURATOM-MECTS/Romania (for MN and IP) and under the contract of Association between EURATOM/Hellenic Republic (for HI, AV and LV), was carried out within the framework of the European Fusion Development Agreement. The views and opinions expressed herein do not necessarily reflect those of the European Commission.

Appendix. Details of the DCT method

In this appendix, we derive the relations that allow us to calculate the diffusion coefficients in the frame of the DCT method. The main idea of the method is to study the Langevin system (11)–(12) not in the whole space of the realizations of the possible fluctuations, but to subdivide the whole space into a set of *subensembles* S , characterized by given values of the potential and of the different fluctuating field components at the starting point of the trajectories. The definition of the approximative DCT method can practically be summarized in the following two statements:

- (i) In each subensemble a deterministic trajectory $x^S(z)$ is defined by the following criterion: the *Eulerian average* of the potential ψ^S in the subensemble S , calculated along this

deterministic trajectory, equals the *Lagrangian* average of the same potential in the subensemble S

$$\psi^S[\mathbf{x}^S(z); z] = \langle \psi[\mathbf{x}(z); z] \rangle^S. \quad (\text{A.1})$$

This deterministic trajectory is called decorrelation trajectory.

- (ii) The average Lagrangian velocity in the subensemble S is approximated with the average Eulerian velocity calculated along the deterministic trajectory.

In the DCT method, we can consider the Lagrangian average of the potential as the corresponding Eulerian average calculated along the deterministic trajectory (i.e. the solutions of the system (11)–(12)) *in the same subensemble*. We first need to calculate the average Eulerian fields in the subensemble S (see equations (A.6) and (A.7)). The next step in the DCT method is to define a deterministic trajectory in each subensemble as a solution of the system (11)–(12), in which the right-hand sides are replaced by the average fields in the subensemble. Inserting these approximations into the exact formula for the Lagrangian field correlation yields an approximation that is valid, in principle, for arbitrarily large values of the different Kubo numbers. The main reason for this to hold is that the DCT method takes into account trapping effects, which are neglected in other approaches that are based on the Corrsin approximation.

The exact expression of the Lagrangian correlation can be written in the form of a superposition of Lagrangian correlations in various subensembles. We define a set of *subensembles* S of the realizations of the stochastic magnetic field by given values of the potential ψ or the characteristic magnetic field fluctuation \mathbf{b} and b_z at the point $\mathbf{x} = 0$ at the ‘moment’ $z = 0$,

$$\psi(\mathbf{0}; 0) = \psi^0, \quad \mathbf{b}(\mathbf{0}; 0) = \mathbf{b}^0, \quad b_z(\mathbf{0}; 0) = b_z^0. \quad (\text{A.2})$$

The probability density for \mathbf{b} , b_z , ψ to assume the values \mathbf{b}^0 , b_z^0 , ψ^0 at $\mathbf{x} = 0$, and at the ‘moment’ $z = 0$ in a subensemble is defined as

$$P(\psi^0, \mathbf{b}^0, b_z^0) = \langle \delta[\psi^0 - \psi(\mathbf{0}; 0)] \delta[\mathbf{b}^0 - \mathbf{b}(\mathbf{0}; 0)] \delta[b_z^0 - b_z(\mathbf{0}; 0)] \rangle \quad (\text{A.3})$$

and after short calculations the probability in the subensemble is found to be

$$P(\psi^0, \mathbf{b}^0, b_z^0) = (2\pi)^{-5/2} \Lambda^{-2} \times \exp\left(-\frac{(\psi^0)^2 + (\Lambda^{-1}b_x^0)^2 + (b_y^0)^2 + (\Lambda^{-1}b_{zx}^0)^2 + (b_{zy}^0)^2}{2}\right). \quad (\text{A.4})$$

The characteristic averages in the subensemble are calculated as

$$\langle \mathbf{b}^S(\mathbf{x}; z) \rangle = [P(\psi^0, \mathbf{b}^0, b_z^0)]^{-1} \times \langle \mathbf{b}(\mathbf{x}; z) \delta[\psi^0 - \psi(\mathbf{0}; 0)] \delta[\mathbf{b}^0 - \mathbf{b}(\mathbf{0}; 0)] \delta[b_z^0 - b_z(\mathbf{0}; 0)] \rangle \quad (\text{A.5})$$

and

$$\langle b_z^S(\mathbf{x}; z) \rangle = [P(\psi^0, \mathbf{b}^0, b_z^0)]^{-1} \times \langle b_z(\mathbf{x}; z) \delta[\psi^0 - \psi(\mathbf{0}; 0)] \delta[\mathbf{b}^0 - \mathbf{b}(\mathbf{0}; 0)] \delta[b_z^0 - b_z(\mathbf{0}; 0)] \rangle.$$

Using expressions (8) and (A.17)–(A.21) (see below), the explicit forms of these averages are

$$\langle b_i^S(\mathbf{x}; z) \rangle = \psi^0 M_{\psi i}(\mathbf{x}; z) + b_j^0 M_{ji}(\mathbf{x}; z) + b_{zj}^0 M_{zj|i}(\mathbf{x}; z), \quad i, j = x, y, \quad (\text{A.6})$$

$$\langle b_{zi}^S(\mathbf{x}; z) \rangle = \psi^0 M_{\psi|zi}(\mathbf{x}; z) + b_j^0 M_{j|zi}(\mathbf{x}; z) + b_{zj}^0 M_{zj|zi}(\mathbf{x}; z), \quad i, j = x, y. \quad (\text{A.7})$$

The global Lagrangian correlations are given as

$$L_{ij}(z) = \int d\psi^0 d\mathbf{b}^0 db_z^0 P(\psi^0, \mathbf{b}^0, b_z^0) \langle v_i(\mathbf{0}; 0) v_j[\mathbf{x}(z); z] \rangle^S \quad (\text{A.8})$$

with the components of $\mathbf{v}[\mathbf{x}(z); z]$ in the form

$$\begin{aligned} v_x(\mathbf{x}; z) &= K_m b_x(\mathbf{x}; z) - K_{\text{dr}} b_{zy}(\mathbf{x}; z), \\ v_y(\mathbf{x}; z) &= \Lambda K_m b_y(\mathbf{x}; z) + \Lambda K_{\text{dr}} b_{zx}(\mathbf{x}; z). \end{aligned} \quad (\text{A.9})$$

The components of the Lagrangian correlation tensor $L_{ij}^S(\psi^0, \mathbf{b}^0, \mathbf{b}_z^0, z) \equiv \langle v_i(\mathbf{0}; 0) \times v_j[\mathbf{x}(z); z] \rangle^S$ in a subensemble are

$$\begin{aligned} L_{xx}^S(\psi^0, \mathbf{b}^0, \mathbf{b}_z^0, z) &= (K_m^2 b_x^0 - K_{\text{dr}} K_m b_{zy}^0) \langle b_x^S(\mathbf{x}; z) \rangle \\ &+ (K_{\text{dr}}^2 b_{zy}^0 - K_m K_{\text{dr}} b_x^0) \langle b_{zy}^S(\mathbf{x}; z) \rangle, \end{aligned} \quad (\text{A.10})$$

$$\begin{aligned} L_{xy}^S(\psi^0, \mathbf{b}^0, \mathbf{b}_z^0, z) &= (K_m^2 b_x^0 - K_{\text{dr}} K_m b_{zy}^0) \langle b_y^S(\mathbf{x}; z) \rangle \\ &- (K_{\text{dr}}^2 b_{zy}^0 - K_m K_{\text{dr}} b_x^0) \langle b_{zx}^S(\mathbf{x}; z) \rangle, \end{aligned} \quad (\text{A.11})$$

$$\begin{aligned} L_{yy}^S(\psi^0, \mathbf{b}^0, \mathbf{b}_z^0, z) &= (K_m^2 b_y^0 + K_{\text{dr}} K_m b_{zx}^0) \langle b_y^S(\mathbf{x}; z) \rangle \\ &+ (K_{\text{dr}}^2 b_{zx}^0 + K_m K_{\text{dr}} b_y^0) \langle b_{zx}^S(\mathbf{x}; z) \rangle, \end{aligned} \quad (\text{A.12})$$

$$\begin{aligned} L_{yx}^S(\psi^0, \mathbf{b}^0, \mathbf{b}_z^0, z) &= (K_m^2 b_y^0 + K_{\text{dr}} K_m b_{zx}^0) \langle b_x^S(\mathbf{x}; z) \rangle \\ &- (K_{\text{dr}}^2 b_{zx}^0 + K_m K_{\text{dr}} b_y^0) \langle b_{zy}^S(\mathbf{x}; z) \rangle. \end{aligned} \quad (\text{A.13})$$

The running diffusion coefficients are calculated as usual:

$$D_{ij}(z) = \int_0^z d\zeta L_{ij}(\zeta) \quad (\text{A.14})$$

while the asymptotic value is given as

$$D_{ij}^{\text{as}} = \lim_{z \rightarrow \infty} D_{ij}(z). \quad (\text{A.15})$$

In section 3, we showed and discussed decorrelation trajectories in different subensembles, and the running diagonal diffusion coefficients presented there are determined according to equation (A.14).

Using equation (8) in a dimensionless form and the antisymmetric tensor ε_{nm} [$\varepsilon_{11} = \varepsilon_{22} = 0$ and $\varepsilon_{12} = -\varepsilon_{21} = 1$], the Eulerian correlations can be written in terms of the magnetic potential and its derivatives [23, 35],

$$M(\mathbf{x}; z) = \exp\left(-\frac{\mathbf{x}^2 + z^2}{2}\right), \quad (\text{A.16})$$

$$\begin{aligned} M_{\psi n}(\mathbf{x}; z) &= \langle \psi(\mathbf{0}; 0) b_n(\mathbf{x}; z) \rangle = \varepsilon_{nm} \frac{\partial M(\mathbf{x}; z)}{\partial x_m} \\ &= -M_{n\psi}(\mathbf{x}; z), \quad n, m = x, y, \end{aligned} \quad (\text{A.17})$$

$$M_{ij}(\mathbf{x}; z) = \langle b_i(\mathbf{0}; 0) b_j(\mathbf{x}; z) \rangle = -\varepsilon_{im} \varepsilon_{jn} \frac{\partial^2 M(\mathbf{x}; z)}{\partial x_m \partial x_n}, \quad n, m = x, y, \quad (\text{A.18})$$

$$\begin{aligned} M_{\psi|zi}(\mathbf{x}; z) &= \langle \psi(\mathbf{0}; 0) b_{zi}(\mathbf{x}; z) \rangle = \varepsilon_{im} \frac{\partial}{\partial z} \left(\frac{\partial M(\mathbf{x}; z)}{\partial x_m} \right) \\ &= M_{zi|\psi}(\mathbf{x}; z), \quad i, m = x, y, \end{aligned} \quad (\text{A.19})$$

$$\begin{aligned} M_{i|zj}(\mathbf{x}; z) &= \langle b_i(\mathbf{0}; 0) b_{zj}(\mathbf{x}; z) \rangle = -\varepsilon_{im} \varepsilon_{jn} \frac{\partial}{\partial z} \left(\frac{\partial^2 M(\mathbf{x}; z)}{\partial x_m \partial x_n} \right) \\ &= -M_{zj|i}(\mathbf{x}; z), \quad n, m, i, j = x, y, \end{aligned} \quad (\text{A.20})$$

$$\begin{aligned}
M_{zi|zj}(\mathbf{x}; z) &= \langle b_{zi}(\mathbf{0}; \mathbf{0}) b_{zj}(\mathbf{x}; z) \rangle = -\varepsilon_{im} \varepsilon_{jn} \frac{\partial^2}{\partial z^2} \left(\frac{\partial^2 M(\mathbf{x}; z)}{\partial x_m \partial x_n} \right) \\
&= M_{zj|zi}(\mathbf{x}; z), \quad n, m, i, j = x, y.
\end{aligned} \tag{A.21}$$

The explicit expressions for the correlations used in this work are easily obtained from equations (8)–(10) and (A.17)–(A.21), and they are the following:

$$M_{\psi x}(\mathbf{x}; z) = -M_{x\psi}(\mathbf{x}; z) = \Lambda \frac{\partial M(\mathbf{x}; z)}{\partial y} = -y\Lambda M(\mathbf{x}; z), \tag{A.22}$$

$$M_{\psi y}(\mathbf{x}; z) = -M_{y\psi}(\mathbf{x}; z) = -\frac{\partial M(\mathbf{x}; z)}{\partial x} = xM(\mathbf{x}; z), \tag{A.23}$$

$$M_{xx}(\mathbf{x}; z) = -\Lambda^2 \frac{\partial^2 M(\mathbf{x}; z)}{\partial y^2} = (1 - y^2)\Lambda^2 M(\mathbf{x}; z), \tag{A.24}$$

$$M_{yy}(\mathbf{x}; z) = -\frac{\partial^2 M(\mathbf{x}; z)}{\partial x^2} = (1 - x^2)M(\mathbf{x}; z), \tag{A.25}$$

$$M_{xy}(\mathbf{x}; z) = M_{yx}(\mathbf{x}; z) = \Lambda \frac{\partial^2 M(\mathbf{x}; z)}{\partial x \partial y} = xy\Lambda M(\mathbf{x}; z), \tag{A.26}$$

$$M_{zx|\psi}(\mathbf{x}; z) = M_{\psi|zx}(\mathbf{x}; z) = \frac{\partial}{\partial z} \left(\frac{\partial M(\mathbf{x}; z)}{\partial y} \right) = zy\Lambda M(\mathbf{x}; z), \tag{A.27}$$

$$M_{zy|\psi}(\mathbf{x}; z) = M_{\psi|zy}(\mathbf{x}; z) = \frac{\partial}{\partial z} \left(-\frac{\partial M(\mathbf{x}; z)}{\partial x} \right) = -zxM(\mathbf{x}; z), \tag{A.28}$$

$$M_{x|zx}(\mathbf{x}; z) = \Lambda^2 \frac{\partial}{\partial z} \left(-\frac{\partial^2 M(\mathbf{x}; z)}{\partial y^2} \right) = -z(1 - y^2)\Lambda^2 M(\mathbf{x}; z) = -M_{zx|x}(\mathbf{x}; z), \tag{A.29}$$

$$\begin{aligned}
M_{y|zx}(\mathbf{x}; z) &= M_{x|zy}(\mathbf{x}; z) = \Lambda \frac{\partial}{\partial z} \left(\frac{\partial^2 M(\mathbf{x}; z)}{\partial x \partial y} \right) = -xyz\Lambda M(\mathbf{x}; z) \\
&= -M_{zy|x}(\mathbf{x}; z) = -M_{zx|y}(\mathbf{x}; z),
\end{aligned} \tag{A.30}$$

$$M_{y|zy}(\mathbf{x}; z) = \frac{\partial}{\partial z} \left(-\frac{\partial^2 M(\mathbf{x}; z)}{\partial x^2} \right) = -z(1 - x^2)M(\mathbf{x}; z) = -M_{zy|y}(\mathbf{x}; z), \tag{A.31}$$

$$M_{zx|zx}(\mathbf{x}; z) = \Lambda^2 \frac{\partial^2}{\partial z^2} \left(\frac{\partial^2 M(\mathbf{x}; z)}{\partial y^2} \right) = (1 - z^2)(1 - y^2)\Lambda^2 M(\mathbf{x}; z), \tag{A.32}$$

$$M_{zy|zx}(\mathbf{x}; z) = M_{zx|zy}(\mathbf{x}; z) = \Lambda \frac{\partial^2}{\partial z^2} \left(\frac{\partial^2 M(\mathbf{x}; z)}{\partial x \partial y} \right) = (1 - z^2)xy\Lambda M(\mathbf{x}; z), \tag{A.33}$$

$$M_{zy|zy}(\mathbf{x}; z) = \frac{\partial^2}{\partial z^2} \left(\frac{\partial^2 M(\mathbf{x}; z)}{\partial x^2} \right) = (1 - z^2)(1 - x^2)M(\mathbf{x}; z), \tag{A.34}$$

$$M_{xy}(\mathbf{x}; z) = M_{yx}(\mathbf{x}; z), \quad M_{\psi|zi}(\mathbf{x}; z) = M_{zi|\psi}(\mathbf{x}; z),$$

$$M_{zy|zx}(\mathbf{x}; z) = M_{zx|zy}(\mathbf{x}; z),$$

$$M_{y|zx}(\mathbf{x}; z) = M_{x|zy}(\mathbf{x}; z) = -M_{zy|x}(\mathbf{x}; z) = -M_{zx|y}(\mathbf{x}; z). \tag{A.35}$$

In the applications, we numerically evaluate the Lagrangian correlation tensor, the running diffusion tensor and also the asymptotic diffusion tensor, using an optimized numerical code based on the Runge–Kutta–Fehlberg 45 (RK45) method, as in [28, 36]. For each Lagrangian correlation tensor a large enough number of decorrelation trajectories are considered, between 31^3 and 35^3 . For each trajectory, a non-uniform grid in time direction, with up to 200 grid points, is used. The final time was chosen between 10 and 15, so that the particles have reached the asymptotic regime. From the numerical point of view, the problem is equivalent to the calculation of an integral of the generic form $\iiint dx dy dz (e^{-\frac{1}{2}(x^2+y^2+z^2)} \cdot f(x, y, z))$. We evaluate the integral as a sum that contains a number of maximum 31 terms, and because of the integrand's form, we can consider the integration limits to be ± 4 instead of $\pm\infty$. After the calculation of the integral, an additional integral over 'time' must be done in order to obtain the components of the running diffusion tensor.

Euraton © 2011.

References

- [1] Liewer P 1985 *Nucl. Fusion* **25** 543
- [2] Balescu R 2005 *Aspects on Anomalous Transport in Plasmas* (Bristol: Institute of Physics Publishing)
- [3] Doyle E J *et al* 2007 *Nucl. Fusion* **47** S18
- [4] Paraïl V *et al* 2009 *Nucl. Fusion* **49** 075030
- [5] Giroud C *et al* and the JET EFDA Contributors 2007 *Nucl. Fusion* **47** 313–30
- [6] Guirlet R *et al* 2009 *Nucl. Fusion* **49** 055007
- [7] Guirlet R, Giroud C, Parisot T, Puiatti M E, Bourdelle C, Carraro L, Dubuit N, Garbet X and Thomas P R 2006 *Plasma Phys. Control. Fusion* **48** B63
- [8] McClements K G and McKay R J 2009 *Plasma Phys. Control. Fusion* **51** 115009
- [9] Wong K L and Cheng C Z 1989 *Phys. Fluids B* **1** 545
- [10] McClements K G 2005 *Phys. Plasmas* **12** 072510
- [11] McClements K G and Thyagaraja A 2007 *Plasma Phys. Control. Fusion* **49** 1415–29
- [12] Angioni C, Dux R, Fable E, Peeters A G and the ASDEX Upgrade Team 2007 *Plasma Phys. Control. Fusion* **49** 2027
- [13] Hein T and Angioni C 2010 *Phys. Plasmas* **17** 012307
- [14] Angioni C, Peeters A G, Pereverzev G V, Bottino A, Candy J, Dux R, Fable E, Hein T and Waltz R E 2009 *Nucl. Fusion* **49** 055013
- [15] Fülöp T and Nordman H 2009 *Phys. Plasmas* **16** 032306
- [16] Sánchez Burillo G, van Milligen B Ph and Thyagaraja A 2010 *Phys. Plasmas* **17** 052304
- [17] Reiser D, Reiter D and Tokar M Z 1998 *Nucl. Fusion* **38** 165
- [18] Giroud C *et al* and the JET-EFDA Contributors 2006 *Proc. 21st Int. Conf. on Fusion Energy 2006 (Chengdu, China, 2006)* (Vienna: IAEA) IAEA-CN-149/EX/8-3 (see the appendix of M L Watkins *et al*)
- [19] Zimbaro G, Veltri P and Pommois P 2000 *Phys. Rev. E* **61** 1940
- [20] Pommois P, Zimbaro G and Veltri P 1998 *Phys. Plasmas* **5** 1288
- [21] Neuer M and Spatschek K H 2006 *Phys. Rev. E* **74** 036401
- [22] Castiglione P 2000 *J. Phys. A: Math. Gen.* **33** 1975
- [23] Negrea M, Petrisor I and Balescu R 2004 *Phys. Rev. E* **70** 046409
- [24] Pommois P, Veltri P and Zimbaro G 2001 *Phys. Rev. E* **63** 066405
- [25] Vlad M, Spineanu F, Misguich J H and Balescu R 1996 *Phys. Rev. E* **53** 5302
- [26] Balescu R, Wang H and Misguich J H 1994 *Phys. Plasmas* **1** 3826
- [27] Fujisawa A, Shimizu A, Nakano H and Ohshima S 2007 *Plasma Phys. Control. Fusion* **49** 845
- [28] Watt H A and Shampine L F 1977 *Subroutine RK45 in Computer Methods for Mathematical Computations* (Englewood Cliff, NJ: Prentice-Hall)
- [29] Lalescu C C, Teaca B and Carati D 2010 *J. Comput. Phys.* **229** 5862–9
- [30] Balescu R 1988 *Transport Processes in Plasmas* vol 1 *Classical Transport* vol 2 *Neoclassical Transport* (Amsterdam: North Holland)
- [31] Wesson J 2004 *Tokamaks* 3rd edn (Oxford: Clarendon) section 3.4

- [32] Vlad M, Spineanu F, Misguich J H and Balescu R 2003 *Phys. Rev. E* **67** 026406
- [33] Negrea M, Petrisor I and Weyssow B 2007 *Plasma Phys. Control. Fusion* **49** 1767–81
- [34] Petrisor I, Negrea M and Weyssow B 2007 *Phys. Scr.* **75** 1
- [35] Hai-Da Wang, Vlad M, Vanden Eijnden E, Spineanu F, Misguich J H and Balescu R 1995 *Phys. Rev. E* **51** 4844
- [36] Forsythe G E, Malcolm M A and Moler C B 1977 *Computer Methods for Mathematical Computations* (Englewood Cliffs, NJ: Prentice-Hall)